Electronic
Research Archive

https://www.aimspress.com/journal/ERA

ERA, 33(9): 5277–5300.
DOI: 10.3934/era.2025236
Received: 18 July 2025
Revised: 16 August 2025
Accepted: 28 August 2025
Published: 05 September 2025

Research article

Nonlinear and ionic mechanisms for bursting patterns and subthreshold resonance in mesencephalic V neurons

Linan Guan[1], Huaguang Gu[2,*] and Xinjing Zhang[1]

[1] School of Mathematics and Statistics, North China University of Water Resources and Electric Power, Zhengzhou 450046, China

[2] School of Aerospace Engineering and Applied Mechanics, Tongji University, Shanghai 200092, China

* **Correspondence:** Email: guhuaguang@tongji.edu.cn.

Abstract: The bursting and subthreshold resonance of mesencephalic trigeminal nucleus neurons play a critical role in bite force control and orofacial pain processing, yet their underlying dynamical mechanisms remain poorly understood. The nonlinear and ionic mechanisms are presented in the present paper. First, bifurcations from the resting state to bursting, modulated by persistent sodium current (I_{NaP}) and applied current (I_{app}), are obtained, including a Hopf bifurcation. Second, three typical bursting patterns are distinguished via codimension-2 bifurcations, and coexisting behaviors are acquired through fast/slow analysis. Modulated by I_{NaP}, the most common bursting pattern, similar to experimental observations, exhibits bursts interrupted by long quiescent states. In the fast subsystem, the limit cycle for the burst is far from the coexisting equilibrium for the quiescent state. Then, stochastic transitions between the two behaviors cannot be evoked, resulting in robustness to noise. Two other bursting patterns manifest transitions between bursts for a large limit cycle and subthreshold oscillation for a small limit cycle. Proximity between the two limit cycles allows noise to drive stochastic transitions, leading to noise-sensitive dynamics. The sensitivity is determined by the distance between the two cycles. Finally, subthreshold resonance evoked from the resting state is reproduced, which is mediated by potassium current. Enhanced I_{NaP} and I_{app} amplify the resonance amplitude and frequency by driving the resting state toward the Hopf bifurcation. The dynamics of bursting and resonance advance the understanding of sensorimotor processing and present potential targets for treating orofacial motor disorders.

Keywords: bursting; subthreshold resonance; bifurcation; coexistence; mesencephalic trigeminal neurons; persistent sodium current

1. Introduction

Nonlinear behaviors of neuronal firing activities play essential roles in identifying brain diseases or brain functions [1]. For example, bursting activity has been linked to major depressive disorder [2], Parkinson's disease [3], and epilepsy [4]. Bursting is often modulated by slow stimulations [5] or slow variables related to multiple ions [6–8], such as calcium ions [9]. Bifurcation analysis and fast-slow dynamics analysis [10] reveal the nonlinear dynamical mechanisms governing bursting activity [11–16], providing crucial insights for understanding brain disorders. For instance, the fast-slow variables separation method is effective in identifying distinct bursting patterns by choosing the slow variable and analyzing the bifurcation types of the fast subsystem [17–20]. Given the ubiquitous presence of noise in neural systems, noise-induced modifications of bursting dynamics have attracted significant research attention [21]. Recently, complex changes in bursting modulated by noise have been explained through fast-slow dynamics analysis [22,23]. Compared to the deterministic bursting, changes occur in the quiescent states/subthreshold oscillations and bursts of stochastic bursting, since the stochastic alternations between bursts and quiescent states/subthreshold oscillations induced by noise appear around a specific phase or bifurcation. Thus, identification of nonlinear mechanisms underlying the bursting is an important issue.

In addition to bursting, subthreshold resonance is a fundamental property in frequency-selective signal processing [24,25]. Resonance emerges when a peak response amplitude appears at a specific stimulation frequency (f_{res}), indicating frequency-selective amplification [26]. Experimental studies have revealed that resonance appears in diverse types of neurons, such as thalamic reticular nucleus neurons [27], pyramidal neurons in the hippocampal CA1 region [28], and neurons in the sensorimotor cortex [29]. Subthreshold resonance improves the capacity to detect rhythmic signals, while aberrant subthreshold resonance may contribute to neurological disorders. For instance, subthreshold resonant characteristics play a role in the encoding of the auditory system [30]. Abnormally increased resonance in thalamocortical circuits and CA1 pyramidal cells may promote synchronized firing and epileptogenesis [26,31]. Neuronal resonance can be mediated by several ion currents, including the hyperpolarization-activated cation current (I_{h}) [32], calcium current (I_{Ca}) [33], low-threshold potassium current (I_{KLT}) [34], and M-type potassium current ($\mathrm{I_M}$) [35]. In addition, some ion currents can regulate the intensity of the resonance. For example, the persistent sodium current (I_{NaP}) can amplify the resonance mediated by $I_{\mathrm{h}}/I_{\mathrm{M}}$ or I_{h} [35,36]. The delayed rectifier potassium current (I_{Kir}) weakens the resonance mediated by I_{h} [29]. In nonlinear dynamics, resonance is closely tied to the type of equilibrium points [37]. It is easy for a stable focus to exhibit resonance, as it has an inherent frequency, whereas the same is difficult for a stable node (which has no inherent frequency). Moreover, resonance triggered by the I_{h} current is closely associated with a Hopf bifurcation [38,39]. Then, the identification of ionic and nonlinear mechanisms underlying resonance is also a significant issue.

Both bursting and subthreshold resonance in the mesencephalic trigeminal sensory neurons (Mes V neurons) play roles in various functions, such as the transmission of orofacial proprioceptive information, mastication, and bite force regulation [40]. For instance, the monosynaptic reflex (e.g., the jaw-jerk reflex) modulates bite force to avoid dental damage [41]. Moreover, abnormal Mes V activity is strongly linked to temporomandibular disorders (TMD) [42], which primarily affect adults, manifesting as pain and motor dysfunction (e.g., sleep bruxism) [43]. For Mes V neurons, the most common bursting exhibits transitions between quiescent states and bursts with multiple high-frequency spikes. Compared to single spikes, bursting exhibits superior noise resistance, thereby enhancing the reliability of bite force control. As the conductance (g_{NaP}) of the persistent sodium current (I_{NaP}) increases, the interburst interval becomes shorter, while burst duration becomes longer [44]. The prolonged burst duration is associated with sleep bruxism and occlusal pain [45]. Therefore, the modulation of bursting by g_{NaP} has significant physiological and dynamical implications. Complementary to bursting patterns, subthreshold resonance in Mes V neurons substantially contributes to signal integration. Through frequency-specific signal amplification via resonance, Mes V neurons may optimize the encoding of muscle length change velocity [46]. The application of riluzole on Mes V neurons to inhibit I_{NaP} significantly reduces the resonance amplitude [47], indicating that I_{NaP} amplifies resonance. As the resting membrane potential depolarizes, the resonance frequency gradually increases [47], indicating that factors modulating the resting membrane potential, such as applied current (I_{app}), can influence IK-mediated resonance. The dynamical mechanisms underlying resonance changes (e.g., bifurcation types) remain poorly understood. Thus, identifying the dynamical and ionic current mechanisms underlying bursting and subthreshold resonance is important for both nonlinear dynamics and physiological function research.

Here, the dynamical and ionic current mechanisms underlying the bursting and subthreshold resonance of Mes V neurons are investigated using a mathematical model. First, under modulation by I_{NaP} and I_{app}, one- and two-parameter bifurcations from the resting state to bursting are identified, including a Hopf bifurcation. Second, using codimension-1 and codimension-2 bifurcations identified via fast-slow analysis, the most common bursting pattern and two other bursting patterns are distinguished. The robustness of the most common bursting pattern to noise arises from the large distance between the coexisting limit cycle and equilibrium. In contrast, the noise sensitivity observed in the other two patterns stems from the relatively small distance between their coexisting limit cycles. Noise cannot induce stochastic transitions between the two coexisting behaviors in the most common bursting pattern, whereas it can in the other two patterns. The I_{NaP}-dependent modifications in bursting characteristics show close agreement with experimental recordings. Finally, enhanced I_{NaP} in conjunction with I_{app} can increase the frequency and amplitude of resonance mediated by potassium current, as the resting state approaches the Hopf bifurcation. The results for bursting provide new insights into the fine regulation of proprioceptive perception in the maxillofacial region, while those for subthreshold resonance provide theoretical evidence for I_{NaP} and I_{app} as tuners of proprioceptive frequency selectivity. This study presents a dynamical framework for understanding sensorimotor encoding in Mes V neurons and suggests potential targets for treating orofacial motor disorders.

2. Models and methods

2.1. Neuronal model

In the present paper, the Mes V neuron model is from the study [44]. Based on the data obtained in the experiment, the model was built. The model is described as follows:

$$C\frac{\mathrm{d}V}{\mathrm{d}t} = -I_{\mathrm{NaT}} - I_{\mathrm{NaP}} - I_{\mathrm{K}} - I_{\mathrm{Leak}} + I_{\mathrm{app}} \tag{1}$$

$$\frac{dn}{dt}=\frac{n_{\infty}(V)-n}{\tau_{\mathrm{K}}(V)} \tag{2}$$

$$\frac{dh_{\mathrm{t}}}{dt}=\frac{h_{\mathrm{t},\infty}(V)-h_{\mathrm{t}}}{\tau_{\mathrm{NaT}}(V)} \tag{3}$$

$$\frac{dh_{\mathrm{p}}}{dt}=\frac{h_{\mathrm{p},\infty}(V)-h_{\mathrm{p}}}{\tau_{\mathrm{NaP}}(V)} \tag{4}$$

where V is the membrane voltage, C is the membrane capacitance, n is the activation gating variable of the K^+ current (I_{K}), and h_t and h_{p} are the inactivation gating variables of the transient Na^+ current (I_{NaT}) and persistent Na^+ current (I_{NaP}), respectively. I_{app} is the applied bias (DC) current (in pA), and I_{Leak} is the leakage current. I_{K}, I_{NaT}, I_{NaP}, and I_{Leak} are described as follows:

$$I_{\mathrm{K}}=g_{\mathrm{K}}n(V-E_{\mathrm{K}}) \tag{5}$$

$$I_{\mathrm{NaT}}=g_{\mathrm{NaT}}m_{\mathrm{t},\infty}(V)h_{\mathrm{t}}(V-E_{\mathrm{Na}}) \tag{6}$$

$$I_{\mathrm{NaP}}=g_{\mathrm{NaP}}m_{\mathrm{p},\infty}(V)h_{\mathrm{p}}(V-E_{\mathrm{Na}}) \tag{7}$$

$$I_{\mathrm{Leak}}=g_{\mathrm{Leak}}(V-E_{\mathrm{Leak}}) \tag{8}$$

where g_{K}, g_{NaT}, g_{NaP}, and g_{Leak} are the conductances (in nS). Definitions for the voltage-dependent steady-state functions n_{∞}, $m_{\mathrm{t},\infty}$, $h_{\mathrm{t},\infty}$, $m_{\mathrm{p},\infty}$, and $h_{\mathrm{p},\infty}$, and the time constants τ are as follows: $n_{\infty}(V)=\frac{1}{1+e^{-\frac{V+43}{3.9}}}$, $\tau_{\mathrm{K}}=4, m_{\mathrm{t},\infty}(V)=\frac{1}{1+e^{-\frac{V+31.3}{4.3}}}, h_{\mathrm{t},\infty}(V)=\frac{1}{1+e^{\frac{V+55}{7.1}}}, \tau_{\mathrm{NaT}}(V)=3,$

$m_{\mathrm{p},\infty}(V)=\frac{1}{1+e^{-\frac{V+50}{6.4}}}, h_{\mathrm{p},\infty}(V)=\frac{1}{1+e^{\frac{V+52}{14}}}, \tau_{\mathrm{Nap}}(V)=1000+\frac{10000}{1+e^{\frac{V+60}{10}}}.$

The parameter values are given as follows: $E_{\mathrm{K}}=-92$ mV, $E_{\mathrm{Na}}=55$ mV, $E_{\mathrm{Leak}}=-60$ mV, $g_{\mathrm{K}}=6$ nS, $g_{\mathrm{NaT}}=12$ nS, $g_{\mathrm{Leak}}=2$ nS, and $C=1$ pF. g_{NaP} and I_{app} are the regulating parameters. The unit of time is ms.

2.2. White noise

Membrane noise is considered and added to Eq (1). Here, a white noise $\xi(t)$ is used, with statistical properties $<\xi(t)>=0$ and $<\xi(t)\xi(t')>=2\mathrm{D}\delta(t-t')$. Here, $<\cdot>$ represents the average, $\delta(\cdot)$ is the Dirac delta function, and D [in units of $(\mathrm{pA})^2$] represents the noise intensity. The present work examines bursting behavior incorporating noise, thereby achieving greater consistency with experimental observations.

2.3. Fast-slow analysis of bursting

Equations (1)–(4) form the full system. In the full system, h_{p} has a large time constant τ_{NaP}, implying that it is a slow variable. Thus, Eqs (1)–(3) and Eq (4) are referred to as the fast subsystem and slow subsystem, respectively. Then, bifurcation analysis with h_{p} as a parameter can be performed in the fast subsystem. The bursting trajectory is then overlaid on the bifurcation diagram, which can serve to characterize both deterministic and stochastic bursting.

2.4. Indicator for characterizing resonance induced by ZAP stimulation from the resting state

Here, a ZAP current stimulus is used to clarify the role of ionic currents in membrane potential resonance. The ZAP current has a constant amplitude and linearly rising frequency, defined as follows:

$$I_{\mathrm{ZAP}}(t) = I_{\mathrm{max}} sin(2\pi f(t)t) \tag{9}$$

where $f(t) = f_{\mathrm{min}} + (f_{\mathrm{max}} - f_{\mathrm{min}})(\frac{t}{\mathrm{T}})$ is the time-dependent frequency, increasing from f_{min} to f_{max} over a time period T. I_{max} is the stimulus amplitude. In the present paper, $I_{\mathrm{max}} = 0.01$ pA, $f_{\mathrm{min}} = 0$ Hz, $f_{\mathrm{max}} = 250$ Hz, and T = 25 s.

When I_{ZAP} is applied to the resting state, $V(t)$ exhibits oscillations. The Fast Fourier Transform (FFT) of $V(t)$ and $I_{\mathrm{ZAP}}(t)$ can then be obtained, denoted as FFT($V(t)$) and FFT($I_{\mathrm{ZAP}}(t)$). The impedance frequency profile is described as follows:

$$\mathrm{Z}(f) = \frac{\mathrm{FFT}(V(t))}{\mathrm{FFT}(I_{\mathrm{ZAP}}(t))} \tag{10}$$

where f represents the frequency. The magnitude of Z(f), denoted as |Z(f)|, is plotted as a function of f, yielding a frequency response curve that enables quantitative analysis of the resonant response. Resonance manifests as a distinct peak at a specific frequency, referred to as the resonance frequency (f_{res}). The peak value of |Z(f)| at the resonance frequency f_{res} is denoted as |Z(f_{res})|.

In addition, |Z(f)| at 0.5 Hz is labeled as |Z(0.5)|. The ratio of |Z(f_{res})| to |Z(0.5)|, referred to as the Q factor, can also be used to quantify resonance strength.

3. Results

3.1. Bifurcations distinguishing the resting state and bursting

3.1.1. Resting state and bursting

The neuronal model successfully reproduces the membrane properties of Mes V neurons. In Figure 1(a), the red line represents the resting state at $I_{\mathrm{app}} = -12$ pA (upper panel), while the black curve shows the bursting at $I_{\mathrm{app}} = 10$ pA (lower panel). The resting membrane potential at $I_{\mathrm{app}} = -12$ pA is −59.37 mV, while the spike amplitude during bursting reaches ~85 mV.

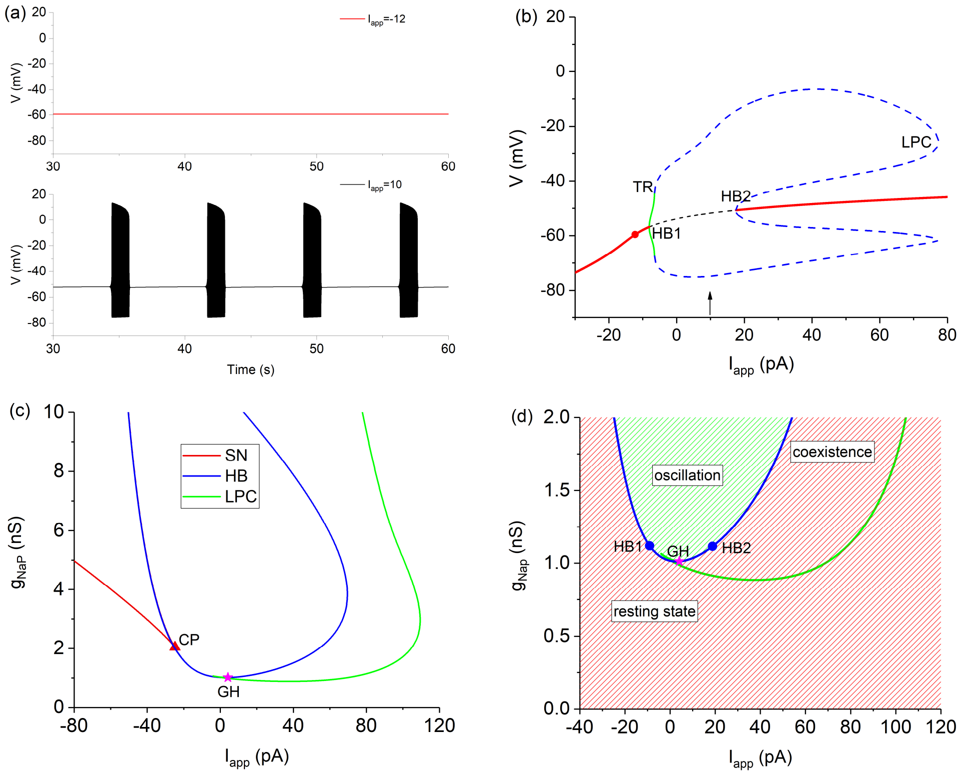

Figure 1. Dynamics related to the resting state and bursting of the full system. (a) Resting state (red line) at $I_{app} = -12$ pA and bursting (black curve) at $I_{app} = 10$ pA, with $g_{NaP} = 1.1$ nS. (b) One-parameter bifurcation diagram. HB1 and HB2 represent Hopf bifurcations. TR and LPC denote Torus bifurcation and limit point bifurcation of limit cycles (LPC), respectively. (c) Two-parameter bifurcation diagram. (d) A magnified view of panel (c). The blue, red, and green curves represent Hopf, saddle-node, and LPC bifurcations, respectively. The red triangle and magenta star represent CP and GH bifurcation points, respectively. The regions marked by red and green diagonal stripes represent the equilibrium and oscillation states, respectively.

3.1.2. One- and two-parameter bifurcations

The resting state can transition to firing (including bursting) via bifurcations. For example, the bifurcations with respect to I_{app} are presented in Figure 1(b). When I_{app} is small, the system remains in a resting state (left red line). The resting state in Figure 1(a) corresponds to the red solid circle in Figure 1(b). As I_{app} increases, a supercritical Hopf bifurcation (HB1) appears at $I_{app} \approx -8.1045$ pA, via which the stable focus (left red) transitions to an unstable focus (black dashed curve), and a stable limit cycle [green curves in Figure 1(b)] emerges, corresponding to subthreshold oscillations with amplitude ~20 mV. The stable limit cycle becomes unstable (blue dashed curve) at $I_{app} = -6.5179$ pA via a torus (TR) bifurcation. The unstable focus transitions to a stable focus (red solid line on the right) via a subcritical Hopf bifurcation (HB2) at $I_{app} \approx 17.4930$ pA, and this stable focus corresponds to a depolarization block state. Via the HB2, another unstable limit cycle (blue dashed curve) emerges, which connects with the previous unstable limit cycle to form a limit point bifurcation of limit cycles (LPC) at $I_{app} \approx 77.3388$ pA. For the parameter domain of unstable limit cycles, bursting behaviors appear (not shown here). For instance, the parameter value of the bursting demonstrated in Figure 1(a) is denoted by the black arrow in Figure 1(b). Thus, the neuron exhibits four distinct dynamical states. Resting state occurs for $I_{\text{app}} < -8.1045$ pA, subthreshold oscillation for $-8.1045 \text{ pA} < I_{\text{app}} < -6.5179$ pA, bursting for $-6.5179 \text{ pA} < I_{\text{app}} < 17.4930$ pA, and depolarization block for $I_{\text{app}} > 17.4930$ pA. As I_{app} increases, the neuronal membrane potential progressively depolarizes, which in turn induces subthreshold oscillations and burst firing. These simulation results are in excellent agreement with experimental observations [47]. In the following analysis, we focus on the resting state and bursting state of neurons. The subthreshold oscillation is confined to a narrow region and is not the focus of the current investigation. More details on subthreshold oscillations are available in the supplementary materials of this paper.

The two-parameter bifurcations in the (I_{app}, g_{NaP}) plane are presented in Figure 1(c), containing two Hopf bifurcation curves (HB, blue), two saddle-node bifurcation curves (SN, red), and an LPC curve (green). Meanwhile, two SN curves coalesce at (24.7651, 2.0431), forming a codimension-2 bifurcation point, Cusp (CP), which is marked by a red triangle. The HB and LPC curves coalesce at the point (4.1764, 1.0119), forming a codimension-2 bifurcation point, generalized Hopf (GH, magenta five-pointed star). A partially enlarged view of Figure 1(c) is shown in Figure 1(d). The regions marked with red diagonal lines and green diagonal lines represent the stable equilibrium point region and the oscillation zone containing bursting, respectively.

3.2. Different bursting patterns modulated by g_{NaP}, I_{app}, and noise

3.2.1. Changes in bursting patterns with respect to g_{NaP} and I_{app}

The interplay between I_{app} and g_{NaP} is capable of producing diverse bursting patterns and modulating bursting properties. Therefore, we selected four representative parameter points in the two-parameter bifurcation diagram to illustrate how I_{app} and g_{NaP} regulate bursting activity, as indicated by the two black dots, one red dot, and one red square in Figure 2(a).

In this model, the slow variable h_{p} of I_{NaP} is the fundamental cause of bursting. Thus, the conductance g_{NaP} affects the characteristics of bursting. When $I_{\text{app}} = 9$ pA, two points represented by red symbols for $g_{\text{NaP}} = 1.25$ nS (representative 1) and 1.1 nS (representative 2) are chosen. For $g_{\text{NaP}} = 1.25$ nS (red square), the bursting cycle consists of two distinct phases: an active burst phase characterized by high-frequency spikes and a resting phase with a long interburst interval, as illustrated in Figure 2(b). The burst duration, interburst interval, burst cycle period, and intraburst spike frequency are 1.964 s, 2.573 s, 4.537 s, and 77.39 Hz, respectively. As g_{NaP} decreases to 1.1 nS (red cycle), the bursting pattern remains unchanged, as shown in Figure 2(e1). The values of the four indicators are 1.212 s, 5.408 s, 6.620 s, and 77.56 Hz, respectively. The enlargement of one period of bursting is shown in Figure 2(e2). The results show that larger g_{NaP} values further prolong the burst duration, shorten the interburst intervals, and consequently reduce the bursting period, while spike frequency within the burst changes little. The results are consistent with experimental observations [44]. This bursting pattern is the most frequently observed in neuronal experiments. The bursting for representatives 1 and 2 belongs to one pattern (called pattern 1 or the common bursting pattern in the present paper).

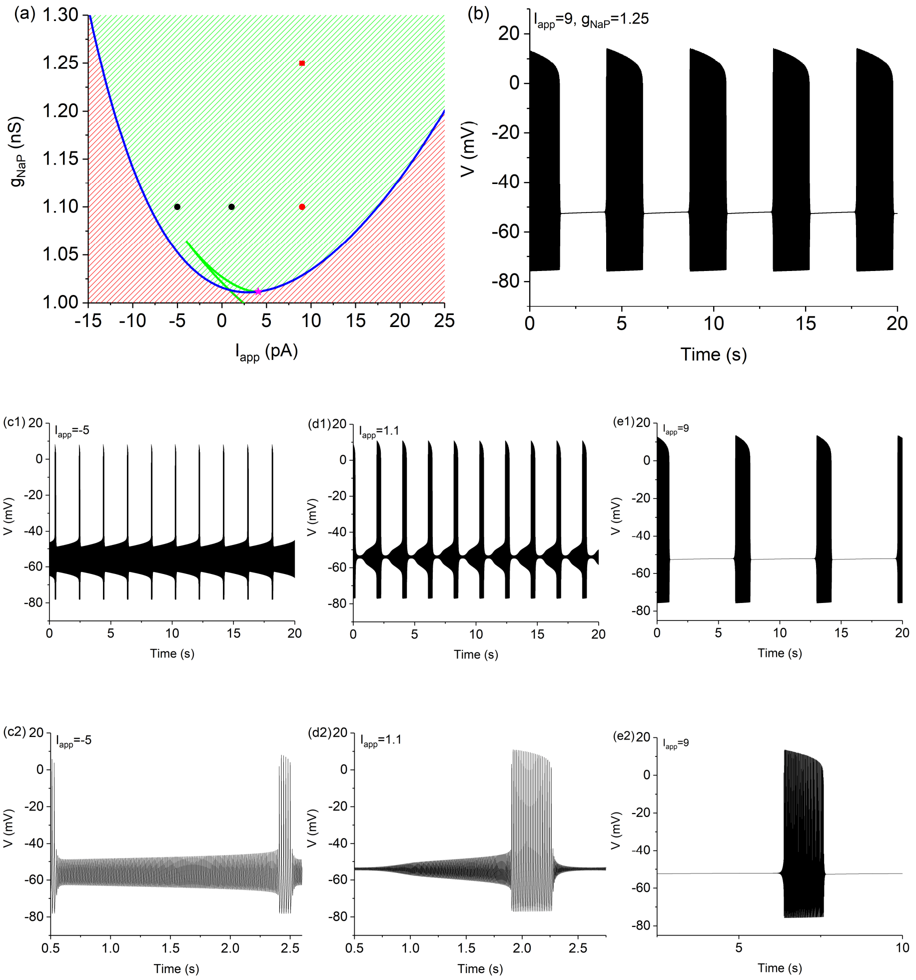

Figure 2. Different bursting patterns. (a) Locations of representative bursting in the magnified view of two-parameter bifurcations [Figure 1(d)]. The time series of bursting: (b) I_{app} = 9 pA and g_{NaP} = 1.25 nS; (c) I_{app} = −5 pA and g_{NaP} = 1.1 nS; (d) I_{app} = 1.1 pA and g_{NaP} = 1.1 nS; (e) I_{app} = 9 pA and g_{NaP} =1.1 nS. Panels (c2), (d2), and (e2) are partial enlarged views of panels (c1), (d1), and (e1), respectively, depicting one bursting period.

When g_{NaP} = 1.1 nS, three different I_{app} values are selected to show the changes in bursting with respect to I_{app}, as indicated by the three dots in Figure 2(a). When I_{app} = −5 pA (representative 3), the burst contains six action potentials, followed by subthreshold oscillations lasting ~1.8 s, as shown in Figure 2(c1). An enlargement of one period of bursting is shown in Figure 2(c2). Such a bursting pattern is called pattern 2. When I_{app} is increased to 1.1 pA (representative 4), more complex bursting patterns emerge, as depicted in Figure 2(d1). The enlargement of one period of bursting is shown in Figure 2(d2). One burst contains 24 spikes, and the subthreshold oscillations (~1.714 s in duration) exhibit increasing amplitude. This bursting pattern is labeled as pattern 3. When I_{app} increases to 9 pA (representative 2), the bursting transitions to pattern 1, as depicted in Figures 2(e1) and (e2). For both pattern 2 and pattern 3, as g_{NaP} increases, the burst duration lengthens, the interburst interval shortens, and the bursting period decreases, exhibiting bursting characteristics similar to those observed in pattern 1. Thus, detailed descriptions are not provided in this paper.

3.2.2. Bursting patterns modulated by noise

To better align the simulation results with experimental observations, Gaussian white noise is considered. For a noise intensity of D = 0.01 (pA)^2, the four representative bursting patterns shown in Figure 2 are illustrated in Figure 3. For pattern 1, while noise induces variations in both bursts and quiescent states, such variations remain minimal. The stochastic bursting retains a largely periodic nature, resembling the experimental observation [47]. Such a regular pattern appears within a broad range of noise intensity, indicating that the bursting pattern is robust against noise. It might also explain why this bursting pattern is observed in experiments. Compared to the deterministic bursting, both the burst duration (intraburst spike counts) and interburst intervals are shortened. For Figure 3(a) corresponding to representative 1, burst duration decreases from 1.964 to 1.476 s, interburst intervals from 2.573 to 1.672 s, and cycle period from 4.537 to 3.148 s. For Figure 3(b), corresponding to representative 2, burst duration decreases from 1.225 to 1.028 s, interburst intervals from 5.395 to 3.439 s, and cycle period from 6.620 to 4.467 s. The underlying mechanism for the robust bursting is addressed in the following subsection using bifurcation analysis.

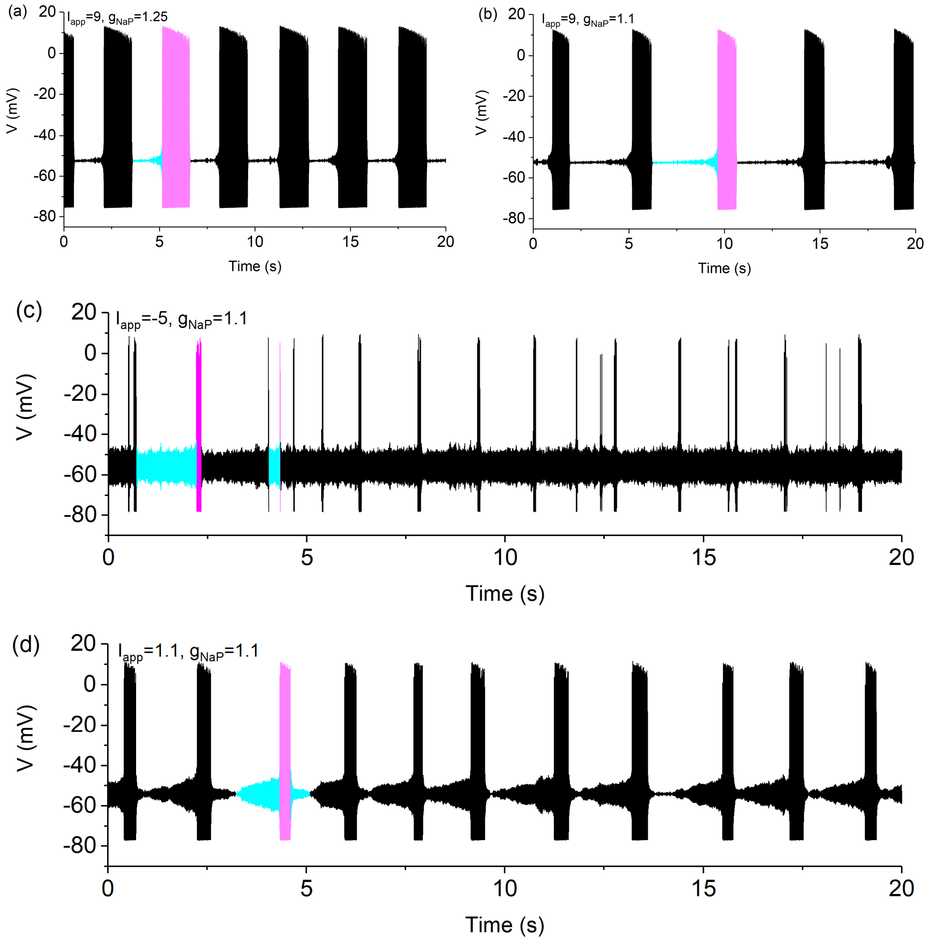

Figure 3. Membrane voltage of stochastic bursting at a noise intensity of D = 0.01 (pA)^2. (a) I_{app} = 9 pA and g_{NaP} = 1.25 nS (representative 1). (b) I_{app} = 9.0 pA and g_{NaP} = 1.1 nS (representative 2). (c) I_{app} = −5 pA and g_{NaP} = 1.1 nS (representative 3). (d) I_{app} = 1.1 pA and g_{NaP} = 1.1 nS (representative 4).

The stochastic bursting for representative 3 exhibits significant variations, with substantial alterations in both subthreshold oscillations and suprathreshold firing phases, as illustrated in Figure 3(c). Individual cycles may contain more or fewer than six spikes, and interburst intervals lengthen or shorten to a large extent. The stochastic bursting appears as irregular behavior. The bifurcation mechanism underlying this bursting is addressed in the following subsection.

For the stochastic bursting corresponding to representative 4, the variations of the burst duration and interburst interval are moderate, smaller than those for representatives 1 and 2, but larger than those for representative 3, as shown in Figure 3(d). Although both the burst duration and subthreshold oscillation duration exhibit variations, the firing periodicity is preserved to a certain extent. Compared to the deterministic bursting pattern [Figure 2(d)], most burst durations (intraburst spike counts) and subthreshold oscillation durations are reduced. The underlying mechanism for the bursting is addressed in the following subsection using bifurcation analysis. For instance, the pink burst in Figure 3(d) comprises 18 spikes, with the subthreshold oscillation period (indicated by the cyan curves) lasting 1.577 s.

3.2.3. Fast-slow analysis of deterministic and stochastic bursting patterns

In this subsection, the dynamical mechanisms underlying the different deterministic and stochastic bursting patterns are obtained through fast-slow analysis. Here, h_{p} is the slow variable, and the bifurcations correspond to the fast subsystem.

For the representative 1 [Figure 2(b)], the bifurcation structure is illustrated in Figure 4(a1). As h_{p} increases, there is a subcritical Hopf bifurcation (subH) at $h_{\mathrm{p}} \approx 0.4149$, and an LPC bifurcation (LPC1) at $h_{\mathrm{p}} \approx 0.3780$. Between the two bifurcations, stable limit cycle (green solid curves) and equilibrium (red solid curve) coexist, separated by the unstable limit cycle (dashed blue curves). The unstable equilibrium point emerging after the subH is illustrated by the black dashed curve. The bifurcations of representative 2 are similar to those of representative 1, as shown in Figure 4(b1). However, the bifurcation points shift rightward, compared to Figure 4(a1). The subH and LPC1 are at $h_{\mathrm{p}} \approx 0.4715$ and 0.4296, respectively. The deterministic bursting pattern can be explained by the bifurcations and coexisting behaviors via superimposing the bursting trajectory (black solid curve) to the (h_{p}, V) plane. For representative 1, the burst phase evolves along the stable limit cycle (green) from right to left, as exhibited in Figure 4(a2), and terminates near the LPC1 point. Then, the trajectory drops to the stable equilibrium, evolves along it initially, and subsequently follows the unstable equilibrium, from left to right, forming the quiescent state phase. Subthreshold oscillations with very short durations occur at the beginning and ending phases of the quiescent state, which are the transient behaviors around the equilibrium, as shown by the left and right inset panels, respectively. The subthreshold oscillations are too short to be found in Figure 2(b). The terminal phase of the quiescent state exhibits a slow passage effect along the unstable equilibrium, attributable to the small real part of the eigenvalue. As the real part becomes large, the phase trajectory transits abruptly to the stable limit cycle (burst phase) to terminate the quiescent phase, as shown in the right inset panel. Therefore, the bursting pattern alternates between the coexisting equilibrium point and limit cycle, which are controlled by the bifurcations, subH, and LPC1. For representative 2, the phase trajectory illustrated in Figure 4(b2) follows the same mechanism as representative 1, which is omitted for brevity. Figure 4 demonstrates that increased g_{NaP} value shortens the parameter range between LPC1 and subH, thereby decreasing the interburst interval. Meanwhile, as g_{NaP} increases, the slow passage phase following the subH becomes long, thus leading to a longer burst duration.

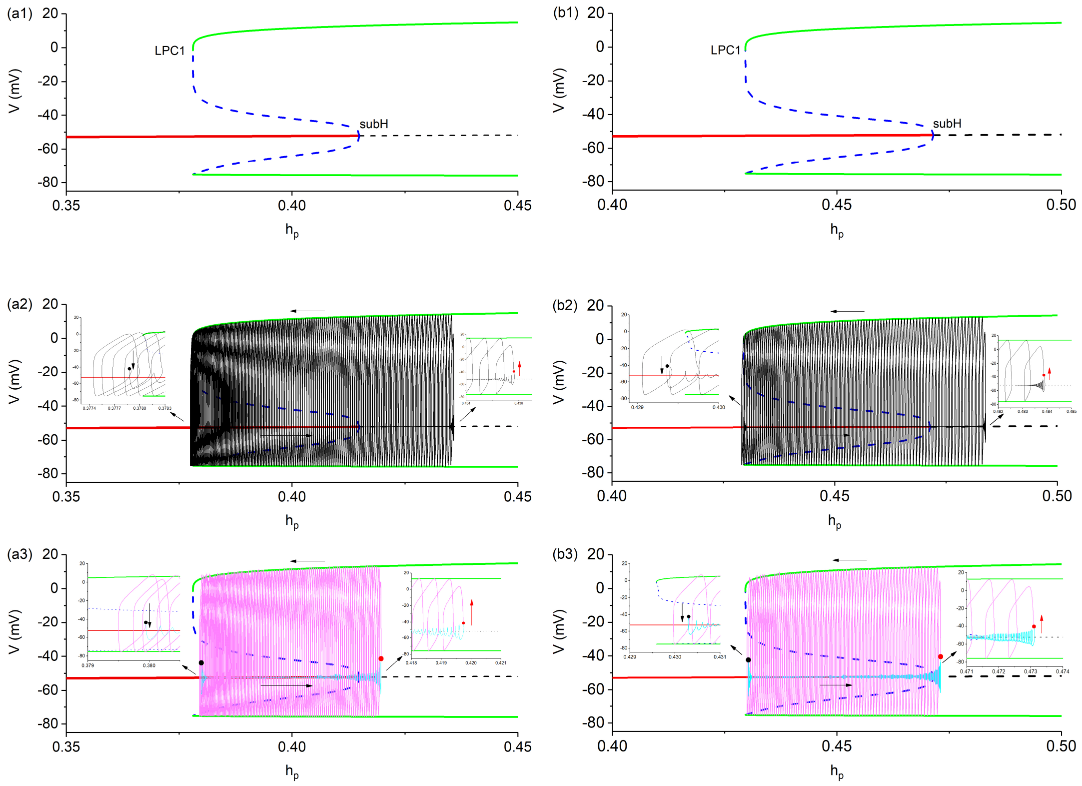

Figure 4. Fast-slow analysis of bursting for pattern 1. Left: $I_{\mathrm{app}} = 9$ pA and $g_{\mathrm{NaP}} = 1.25$ nS (Representative 1). Right: $I_{\mathrm{app}} = 9.0$ pA and $g_{\mathrm{NaP}} = 1.1$ nS (Representative 2). (a1) and (b1) Bifurcations of fast subsystem. (a2) and (b2) Fast-slow analysis of deterministic bursting. The black curves represent the phase trajectories of bursting, and other elements are the same as those in the upper panels. (a3) and (b3) Fast-slow analysis of stochastic bursting. The pink and cyan curves represent the burst phase and resting phase of stochastic bursting. The red and black solid circles represent the switching points of phase trajectories. Inserted panels in the middle and bottom rows represent local enlargements.

The stochastic bursting pattern can also be systematically explained through bifurcation analysis and the characterization of coexisting attractors. For representative 1, the phase trajectory with noise [the burst in Figure 3(a)] is illustrated in Figure 4(a3). Two most pronounced effects of noise can be observed. First, the transition phase from equilibrium to bursting approaches the subcritical Hopf (subH) point, consequently weakening the slow passage effect that typically follows the subH bifurcation, as shown in the right insert panel. Then, the quiescent state terminates early, showing that noise facilitates the departure from the equilibrium point, since noise enhances the oscillations around the quiescent state. The other is that the transition phase from burst to equilibrium advances slightly, compared to the LPC1 point, as shown in the left insert panel. Then, the burst terminates earlier, indicating that noise facilitates the departure from the stable limit cycle, given its proximity to the unstable limit cycle. As the stable limit cycle becomes far from the LPC1, it also becomes far from the unstable one. Then, the departure becomes difficult. Consequently, both the quiescent phase (interburst interval) and burst phase durations decrease, leading to a reduction in the overall bursting period. Representative 2 shares the same mechanism as representative 1. So, a detailed explanation for it is omitted here.

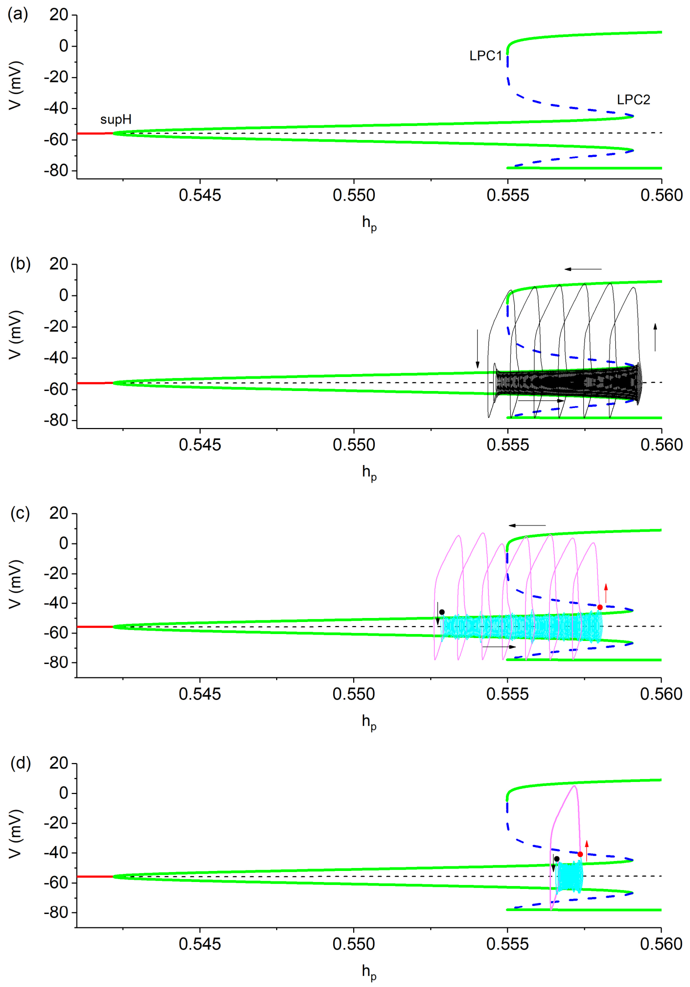

Figure 5. Fast-slow variable analysis of representative 3 bursting for $I_{\mathrm{app}} = -5$ pA and $g_{\mathrm{NaP}} = 1.1$ nS. (a) Bifurcation diagrams of the fast subsystem. (b) The phase trajectory (black curve) of deterministic bursting is overlaid on panel (a). (c) The phase trajectories of stochastic bursting are overlaid on Figure 5(a): The former subthreshold oscillations (cyan) and burst (pink) in Figure 3(c). (d) The latter subthreshold oscillations (cyan) and burst (pink) in Figure 3(c). The curves and solid circles in this figure have the same meanings as those in Figure 4.

For representative 3, the bifurcations are illustrated in Figure 5(a). The stable equilibrium (left red curve) transforms into an unstable one (black dashed curve) through a supH at $h_{\mathrm{p}} \approx 0.5422$. The stable limit cycle (green curves with small amplitude) that bifurcates from the supH transforms into an unstable one (blue dashed curve) via an LPC (LPC2, $h_{\mathrm{p}} \approx 0.5591$). Then, the unstable limit cycle transforms into a stable one (green curve with large amplitude) through another LPC (LPC1, $h_{\mathrm{p}} \approx 0.5550$). Between LPC1 and LPC2, there are coexisting oscillation patterns. One is spiking, and the other is subthreshold oscillation, separated by the unstable limit cycle (blue curve), which determines the noise-modulated dynamics. Phase trajectory of deterministic bursting in Figure 2(c1) (black solid curve) evolves between LPC1 and LPC2, as illustrated in Figure 5(b). The subthreshold oscillations run on the subthreshold (low amplitude) limit cycle from left to right. After running across LPC2, the phase trajectory jumps to and runs on the spiking limit cycle, from right to left. After running across LPC1, the phase trajectory drops back to the subthreshold limit cycle. Therefore, this bursting pattern is formed by two LPC bifurcation points, causing the phase trajectory to switch between the two limit cycles. Compared with representative 1, the distance between the coexisting behaviors is shorter. Consequently, noise can induce more transitions between two coexisting behaviors, which is addressed in the following paragraph.

For representative 3, stochastic bursts with variations can be explained by bifurcations and coexisting behaviors, and the bursts contain different numbers of spikes (>6 or <6). Here, two types of bursts and their corresponding subthreshold oscillations are addressed. One is the former burst and its long subthreshold oscillations, marked in color in Figure 3(c). This burst contains 7 spikes, as shown in Figure 5(c). The other is the latter burst and its short subthreshold oscillations, labeled in color in Figure 3(c). This burst contains one spike, as depicted in Figure 5(d). As shown in Figure 5(c), the initial phases of the burst and subthreshold oscillations occur earlier compared with the deterministic trajectory [Figure 5(b)]. The initial phase of the burst advances, as shown in Figure 5(d), whereas the onset of subthreshold oscillations is delayed, compared to the deterministic case [Figure 5(b)]. The results reveal that stochastic transitions between the spiking and subthreshold limit cycles are frequently induced by noise, given that the spiking limit cycle is close to the subthreshold one.

For representative 4, the supH shifts to a position between LPC1 and LPC2, as shown in Figure 6(a). The bifurcation points for LPC1, supH, and LPC2 are at $h_\mathrm{p} \approx 0.4904$, 0.4933, and 0.5042, respectively. Similar to representative 3, the deterministic bursting (black) manifests a transition between the spiking limit cycle and subthreshold oscillations composed of two parts: one around the stable equilibrium and the other on the subthreshold limit cycle, as shown in Figure 6(b). The burst occurs between LPC1 and LPC2. Differing from representative 3, the amplitude of subthreshold oscillations becomes smaller, especially when it is running across the supH. Then, the stochastic transitions between the spiking limit cycle and subthreshold oscillations induced by noise become difficult, compared with representative 3. The phase trajectory initially evolves along the equilibrium point (the resting phase), as illustrated in Figure 6(b). With noise present, the phase trajectory operating on the small-amplitude limit cycle remains relatively unaffected. Thus, the trajectory transitions to the spiking limit cycle after passing LPC2. However, during its evolution along the spiking limit cycle, noise readily induces sudden transitions back to the equilibrium point or small-amplitude limit cycle, thereby prematurely terminating the burst, as exhibited in Figure 6(c). Consequently, noise narrows the operating parameter range of phase trajectories in both suprathreshold and subthreshold regimes. Therefore, noise decreases both burst durations and interburst intervals.

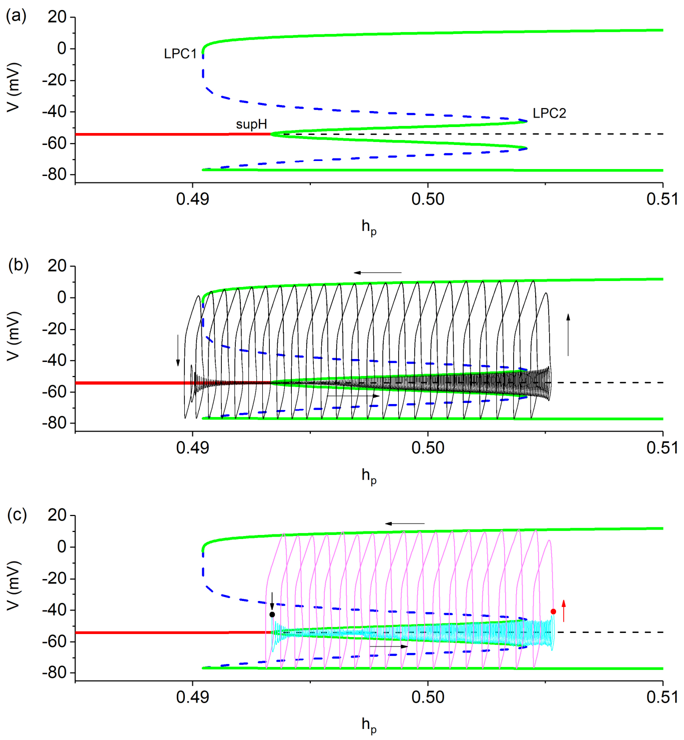

Figure 6. Fast-slow variable analysis of representative 4 bursting for $I_{app} = 1.1$ pA and $g_{NaP} = 1.1$ nS. (a) Bifurcations of the fast subsystem. (b) The phase trajectory (black curve) of deterministic bursting is overlaid on panel (a). (c) The phase trajectory of stochastic bursting is overlaid on panel (a). The pink and cyan curves represent the burst and subthreshold oscillations in Figure 3(d). The curves and solid circles in this figure have the same meanings as those in Figure 4.

3.2.4. Two-parameter bifurcations of the fast subsystem

For the fast subsystem, the two-parameter bifurcations are illustrated in Figure 7, which can provide a more comprehensive explanation of the three bursting patterns. When $g_{NaP} = 1.1$ pA, the bifurcations in the (h_p, I_{app}) plane are illustrated in Figure 7(a). When $I_{app} > 8.4362$ pA (green dashed line), as h_p increases, there is an LPC (LPC1, olive curve) and a subH (cyan solid curve). The bursting pattern 1 appears. Around $I_{app} \approx 8.4362$ pA, the subH transitions to a supH (blue curve), and another LPC (LPC2, green curve) emerges via a codimension-2 bifurcation (GH, magenta triangles). Then, when $0.3167 \text{ pA} < I_{app} < 8.4362$ pA, the supH is located between LPC1 and LPC2, resulting in the bursting pattern 3. When $-6.5179 \text{ pA} < I_{app} < 0.3167$ pA, the supH moves to the left of LPC1, corresponding to the bursting pattern 2. Therefore, as I_{app} increases, changes in the types and positions of the bifurcations induce transitions between the bursting patterns. Subthreshold oscillations and the resting state appear for $I_{app} < -6.5179$ pA. Meanwhile, Figure 7(a) reveals that with increasing I_{app}, the distance between the LPC1 and LPC2 bifurcation points expands. This expanded parameter range enables the phase trajectory to generate more spikes when it operates between these bifurcation points. Thus, the spike counts per burst increase, as I_{app} increases [Figure 2(c1)–(e1)].

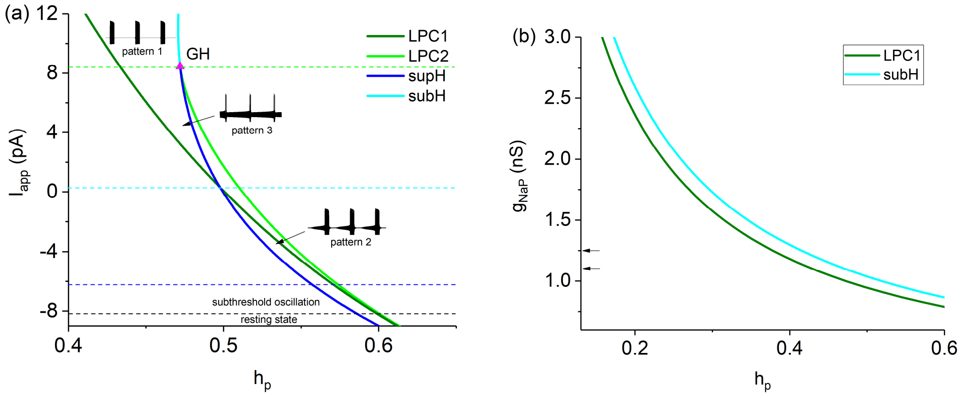

Figure 7. Two-parameter bifurcations in different planes of the fast subsystem. (a) In the (h_p, I_{app}) plane for g_{NaP} = 1.1 nS. (b) In the (h_p, g_{NaP}) plane for I_{app} = 9 pA. GH, marked with a magenta triangle, is a generalized Hopf bifurcation point. The two black arrows indicate the value points for representative 1 and representative 2.

When I_{app} = 9 pA, the two-parameter bifurcations in the (h_p, g_{NaP}) plane are shown in Figure 7(b). As g_{NaP} increases, the LPC2 bifurcation curve is always to the left of the subH curve, indicating that the bifurcation structure does not change with increasing g_{NaP}. Therefore, the g_{NaP} only affects the characteristics of bursting without altering the bursting pattern.

3.3. Dynamics of subthreshold resonance induced from the resting state

3.3.1. The subthreshold resonance mediated by I_K

In this subsection, we primarily investigate the effects of g_{NaP} and I_{app} on subthreshold resonance, thus focusing on the parameter region of the resting state. Figure 8(a) is a partial close-up view of Figure 1(d), and the region (marked by red diagonal lines) corresponds to the resting state. Seven points marked by red squares, blue squares, and a black circle in Figure 8(a) are selected as representatives to study the subthreshold resonance. When g_{NaP} = 0.8 nS, g_K = 6 nS, and I_{app} = −10 pA, the behavior corresponds to a resting state associated with a stable focus, as illustrated by the solid black circle in Figure 8(a). Subthreshold resonance is evoked using a ZAP current sweeping from 0 to 250 Hz over 25 s, as exhibited in Figure 8(c). The membrane voltage amplitude first increases and then decreases after the neuron receives the ZAP current with an amplitude of 0.1 pA, as illustrated in Figure 8(b). This indicates the occurrence of noticeable resonance behavior. With increasing stimulation frequency, the amplitude of the impedance curve increases initially and decreases subsequently, reaching a maximum value at ~76.16 Hz, which means the resonance frequency is approximately 76.16 Hz.

To investigate the effect of potassium current (I_K) on resonance, the potassium conductance g_K is decreased from 6 to 0 nS while g_{NaP} = 0.8 nS and I_{app} = −10 pA. It can be found that the maximum value of the impedance profile increases. However, the impedance profile decreases monotonically with increasing frequency, as illustrated in Figure 9(b). The amplitude of the membrane voltage decreases monotonically with time, as exhibited in Figure 9(a), indicating the absence of resonance. These simulation results align with the experimental data [44], demonstrating that I_K mediates resonance in Mes V neurons.

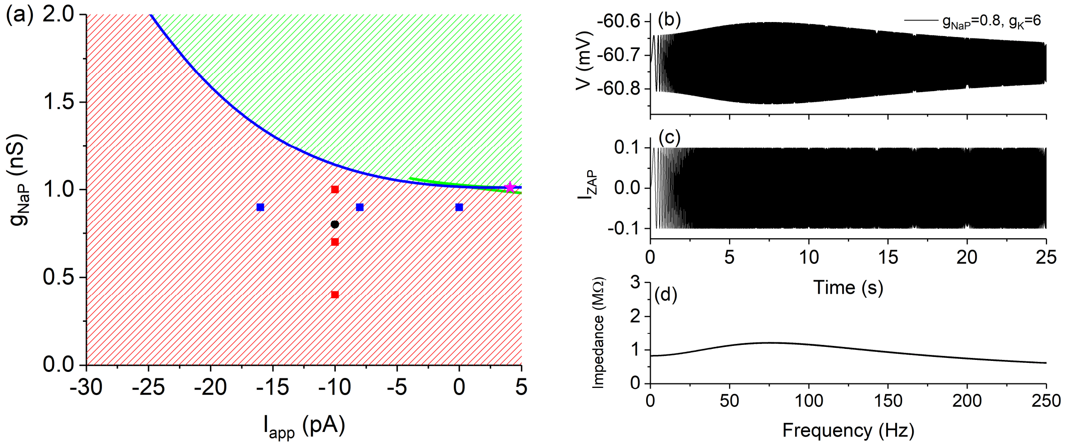

Figure 8. Two-parameter bifurcation in the (I_{app}, g_{NaP}) plane and subthreshold resonance. (a) A partial enlarged view of Figure 1(d). The solid red squares, solid blue squares, and solid black circle indicate the selected different parameter points. (b) Membrane voltage. (c) ZAP stimulation. (d) Impedance profile. g_{NaP} = 0.8 nS, g_K = 6 nS, and I_{app} = −10 pA.

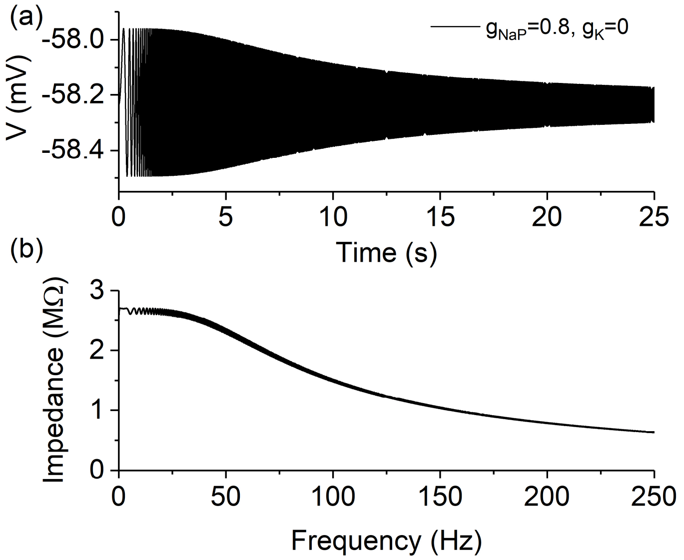

Figure 9. Time series of membrane voltage and impedance profile under ZAP stimulation. (a) Membrane voltage. (b) Impedance profile. g_{NaP} = 0.8 nS, g_K = 0 nS, and I_{app} = −10 pA.

3.3.2. The resonance frequency and intensity (Q factor) increase with increasing g_{NaP} and I_{app}

In the presence of I_K, the neuron generates resonance when subjected to ZAP current stimulation. To further elucidate the impact of g_{NaP} on subthreshold resonance, we selected three representative parameter values from the stable equilibrium region in Figure 8(a) (marked by the solid red squares). As shown in Figure 10(a1), when g_{NaP} = 0.4 nS, the membrane voltage first increases and then decreases, indicating the occurrence of subthreshold resonance. The maximum values of the membrane voltage and impedance profile occur at approximately 6.772 s and 67.72 Hz, respectively. The relatively small oscillation amplitude (0.13 mV) of the membrane potential during the resonance indicates weaker subthreshold resonance. When g_{NaP} increases to 0.7 nS, the resonance frequency is approximately 73.76 Hz, and the maximum amplitude of the membrane voltage for resonance is about 0.2 mV, as shown in Figure 10(b1). When g_{NaP} is further increased to 1.0 nS, the resonance frequency is approximately 80.24 Hz, and the maximum amplitude for resonance increases to about 0.56 mV, as shown in Figure 10(c1). At the same time, when g_{NaP} is 0.4, 0.7, and 1.0 nS, the maximum impedance values are 0.659, 0.974, and 2.800 MΩ, respectively, as demonstrated in Figure 10(a2)–(c2). The Q factors at these three g_{NaP} values are 1.10, 1.29, and 2.95, respectively. It indicates that the resonance frequency and intensity (Q factor) increase as g_{NaP} increases.

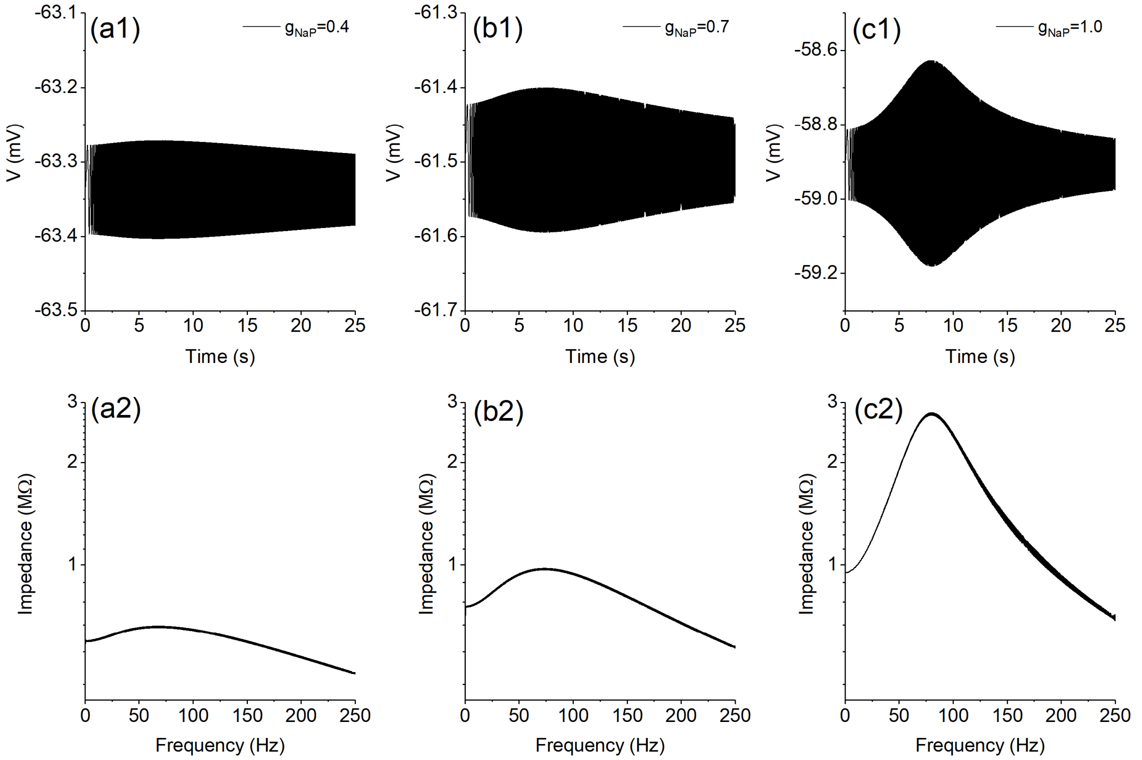

Figure 10. Time series of membrane voltage and impedance profiles under ZAP stimulation. (a) g_{NaP} = 0.4 nS. (b) g_{NaP} = 0.7 nS. (c) g_{NaP} = 1.0 nS. g_K = 6 nS and I_{app} = −10 pA.

Beyond the role of g_{NaP} in resonance properties, I_{app} similarly affects resonance behavior. For g_{NaP} = 0.9 nS and g_K = 6 nS, we analyzed how I_{app} modulates resonance characteristics, as shown in Figure 11(a1). When I_{app} = −16 pA, the membrane voltage amplitude increases at first and subsequently decreases. The membrane voltage reaches its maximum value at 5.353 s, corresponding to resonance occurring at ~53.53 Hz. The maximum voltage amplitude is about 0.2 mV. When I_{app} increases to −8 pA, the resonance frequency is approximately 87.40 Hz, and the maximum amplitude for resonance is about 0.42 mV, as depicted in Figure 11(b1). As I_{app} further increases to 0 pA, the resonance frequency is approximately 129.60 Hz, and the maximum amplitude during resonance increases to about 0.87 mV, as shown in Figure 11(c1). Therefore, the resonance frequency and amplitude increase with increasing I_{app}. As exhibited in Figure 11(a2)–(c2), the maximum impedance values corresponding to I_{app} = −16, −8, and 0 pA are 0.954, 2.103, and 4.361 MΩ, respectively. The Q factors at these three I_{app} values are 1.08, 2.68, and 11.25, respectively. It indicates that the resonance intensity increases as I_{app} increases. Thus, the resonance frequency and intensity (Q factor) increase with the increase of I_{app}.

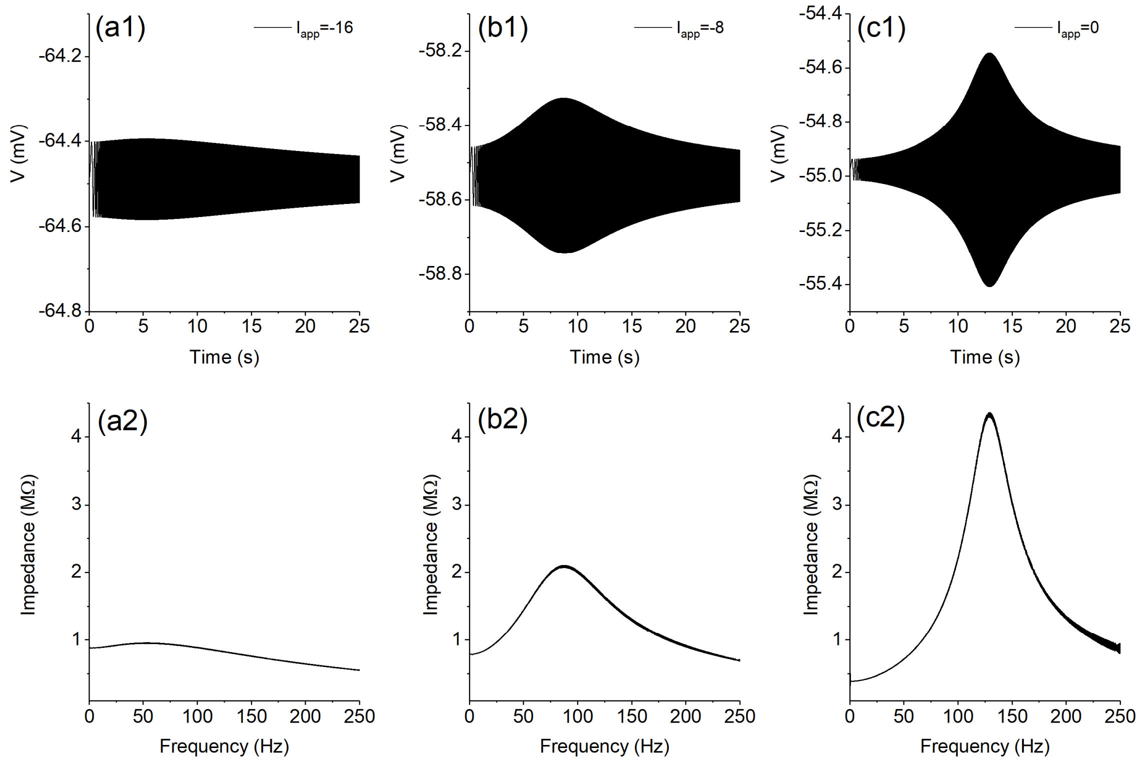

Figure 11. Time series of membrane voltage and impedance profiles under ZAP stimulation. (a) $I_{\mathrm{app}} = -16$ pA. (b) $I_{\mathrm{app}} = -8$ pA. (c) $I_{\mathrm{app}} = 0$ pA. $g_{\mathrm{NaP}} = 0.9$ nS and $g_{\mathrm{K}} = 6$ nS.

3.3.3. The dependence of resonance frequency and intensity (Q factor) on g_{NaP}, I_{app}, and bifurcations

To better elucidate the integrated impact of g_{NaP} and I_{app} on the resonance characteristics, we systematically quantified the distributions of both resonance frequency and Q factor (resonance intensity) across the (I_{app}, g_{NaP}) plane, as exhibited in Figure 12. Color coding in Figure 12 changes from blue to red, representing that the resonance frequency and Q factor increase from low to high. Obviously, with the increase in I_{app} and g_{NaP}, the resonance frequency and intensity exhibit the same trend of variation. For example, when $g_{\mathrm{NaP}} = 0.8$ nS, as I_{app} increases from -18 to 2 pA, the resonance frequency increases from 44.88 to 134 Hz. Meanwhile, the Q factor (resonance intensity) increases from 1.03 to 6.84. Similarly, an increase in g_{NaP} also leads to higher resonance frequency and intensity. Compared to I_{app}, the resonance frequency exhibits a less pronounced dependence on g_{NaP}, as illustrated in Figure 12(a). For $I_{\mathrm{app}} = -10$ pA, as g_{NaP} rises from 0.2 to 1.1 nS, the resonance frequency shifts from 64.56 to 82.20 Hz, while the Q factor grows from 1.06 to 10.17. Therefore, the resonance frequency and intensity increase with increasing I_{app} and g_{NaP}.

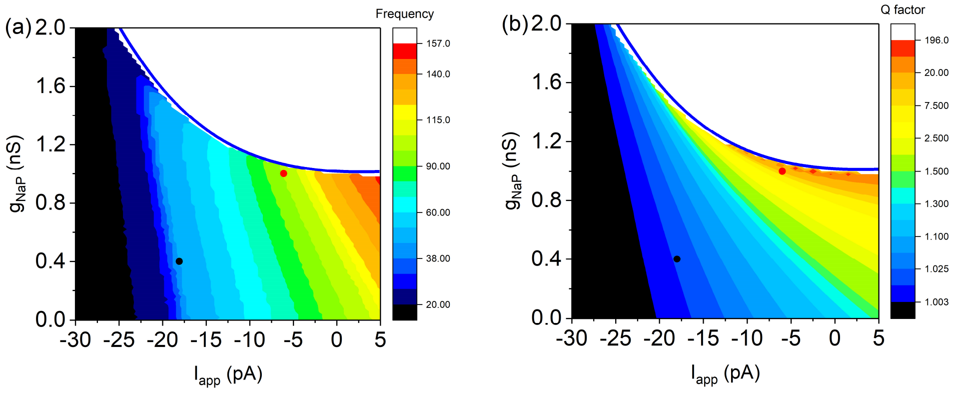

Figure 12. Resonance frequency and Q factor in the (I_{app}, g_{NaP}) plane for $g_K = 6$ nS. (a) Resonance frequency. (b) Q factor. Colors ranging from blue to red correspond to increasing values. The black-colored parameter space indicates no resonant response. The blue curve denotes the Hopf bifurcation curve.

In Figure 12, the blue curve denotes the Hopf bifurcation curve, while the resting state (color region) is positioned to the left of this Hopf bifurcation curve. Weak resonance intensity and low resonance frequency are observed when the equilibrium point is far from the Hopf bifurcation curve. For example, when $I_{app} = -18$ pA and $g_{NaP} = 0.4$ nS (black solid circle), the resonance frequency and Q factor are only 41.08 Hz and 1.01, respectively. At the parameter values near the Hopf bifurcation ($I_{app} = -6$ pA, $g_{NaP} = 1.0$ nS; red solid circle), the system displays pronounced resonance, with a frequency of 101.96 Hz and a Q factor of 10.75. For an equilibrium point near the Hopf bifurcation curve, its eigenvalue has a small real part, resulting in weak damping. This causes the system to exhibit a stronger response when subjected to external stimuli. However, when the equilibrium point approaches the Hopf bifurcation, the imaginary part of its eigenvalue increases, resulting in a higher resonance frequency. For instance, at $I_{app} = 3$ pA, increasing g_{NaP} from 0.5 to 1.0 nS (closer to the Hopf bifurcation curve) causes the imaginary part of the eigenvalues to increase from 0.428171 to 0.748797. Therefore, as g_{NaP} and I_{app} increase, the equilibrium point gradually approaches the Hopf bifurcation curve, thereby leading to enhanced resonance. Therefore, the resonance frequency and intensity (Q factor) increase with the increase of I_{app} and g_{NaP}.

4. Conclusions

The dynamical and ionic current mechanisms that underlie the bursting patterns and subthreshold resonance in mesencephalic trigeminal nucleus (Mes V) neurons are revealed through fast-slow analysis and two-parameter bifurcations. Applied current (I_{app}) initiates state transitions from the resting to subthreshold oscillations via Hopf bifurcation and subsequently to bursting, establishing three distinct patterns of bursting. Using the fast-slow variable separation method, codimension-1 and -2 bifurcations and coexisting behaviors are obtained. Also, the dynamical mechanisms governing the three deterministic bursting patterns and their stochastic counterparts under noise perturbation are acquired. Pattern 1, observed in experiments, exhibits greater robustness. The persistent sodium current (I_{NaP}) acts as a critical regulator of slow variable dynamics, precisely tuning the interburst interval and burst duration. Notably, I_{NaP} and I_{app} induce a Hopf bifurcation that amplifies neural resonance. For instance, elevated g_{NaP} and I_{app} lead to an increase in the resonant frequency. The pathological correlation is particularly significant, as I_{NaP}-mediated shifts toward higher resonance frequencies correspond to aberrant bursting patterns observed in sleep bruxism, suggesting novel therapeutic targeting strategies. These results fundamentally advance our understanding of resonance-burst coupling in sensorimotor processing while providing a robust theoretical framework for developing precision interventions in orofacial motor disorders.

Furthermore, the decreased excitability and disrupted bursting patterns of Mes V neurons are associated not only with orofacial motor disorders (e.g., sleep bruxism) but also neurodegenerative diseases, such as amyotrophic lateral sclerosis (ALS). In transgenic ALS mice, the irregular firing of Mes V neurons induces asynchronous discharges in trigeminal motor neurons (TMNs), corresponding to the early muscle fasciculations [48]. In addition, the resonant behavior of Mes V neurons would be useful for rapid synchronization and stabilization of coordinated activity within the trigeminal network [47]. Changes in ionic conductances, such as g_{NaP}, can alter the frequency preference of Mes V neurons receiving synaptic inputs and their outputs to trigeminal motor neurons, which may in turn affect the pattern of mandibular movement during orofacial motor activities. Thus, the present study carries substantial significance for facilitating the precise encoding and transmission of orofacial proprioceptive signals, thereby safeguarding the functional synchrony of the sensorimotor circuit.

This study primarily focuses on the dynamics of complex firing patterns and subthreshold resonance in single neurons, which will provide valuable insights for future research on the dynamics of trigeminal networks. Since Mes V neurons are electrically coupled, their enhanced resonant properties facilitate synchronized firing patterns among these neurons, thereby enabling their participation in oral-motor pattern generation. Within neuronal networks, complex bursting patterns also undergo complex variations, such as from spiking to bursting in a chain network, involving the cooperation between coupling dynamics and neuronal dynamics [49]. How bursting activity and subthreshold resonance modulate neuronal firing activity at the network level, as well as the underlying dynamical mechanisms, remains an open question. More importantly, further research is required to determine how the effects of various ionic conductances on intrinsic membrane properties and postsynaptic responses of Mes V neurons are integrated. Therefore, future investigations should focus on verifying the frequency-specific modulation mechanisms and their roles in orofacial movements, as well as integrating these mechanisms with synaptic plasticity processes at the network level.

Use of AI tools declaration

The authors declare they have not used Artificial Intelligence (AI) tools in the creation of this article.

Acknowledgments

This work was supported by the National Natural Science Foundation of China (Grant Nos. 12202146, 12372063, and 12202147).

Conflict of interest

The authors declare there is no conflict of interest.

References

1. J. Li, Y. Xie, Y. Yu, M. Du, R. Wang, Y. Wu, A neglected GABAergic astrocyte: Calcium dynamics and involvement in seizure activity, *Sci. China Technol. Sci.*, **60** (2017), 1003–1010. https://doi.org/10.1007/s11431-016-9056-2
2. Y. Cui, Y. Yang, Z. Ni, Y. Dong, G. Cai, A. Foncelle, et al., Astroglial Kir4.1 in the lateral habenula drives neuronal bursts in depression, *Nature*, **554** (2018), 323–327. https://doi.org/10.1038/nature25752
3. H. Zhou, X. Wang, H. Gu, Y. Jia, Deep brain stimulation-induced two manners to eliminate bursting for Parkinson's diseases: synaptic current and bifurcation mechanisms, *Cognit. Neurodyn.*, **19** (2025), 78. https://doi.org/10.1007/s11571-025-10267-5
4. M. L. Saggio, V. Jirsa, Bifurcations and bursting in the Epileptor, *PLoS Comput. Biol.*, **20** (2024), e1011903. https://doi.org/10.1371/journal.pcbi.1011903
5. Q. Xu, Y. Fang, H. Wu, H. Bao, N. Wang, Firing patterns and fast–slow dynamics in an N-type LAM-based FitzHugh–Nagumo circuit, *Chaos, Solitons Fractals*, **187** (2024), 115376. https://doi.org/10.1016/j.chaos.2024.115376
6. Z. Wang, X. Wei, L. Duan, Regulatory mechanism of inhibitory interneurons with time-delay on epileptic seizures under sinusoidal sensory stimulation, *Cognit. Neurodyn.*, **19** (2025), 37. https://doi.org/10.1007/s11571-025-10227-z
7. X. Han, Q. Bi, P. Ji, J. Kurths, Fast-slow analysis for parametrically and externally excited systems with two slow rationally related excitation frequencies, *Phys. Rev. E*, **92** (2015), 012911. https://doi.org/10.1103/PhysRevE.92.012911
8. L. Duan, X. Chen, L. Xia, Z. Wang, Dynamics and control of mixed bursting in nonlinear pre-Bötzinger complex systems, *Nonlinear Dyn.*, **112** (2024), 8539–8556. https://doi.org/10.1007/s11071-024-09473-3
9. J. E. Rubin, J. A. Hayes, J. L. Mendenhall, C. A. Del Negro, Calcium-activated nonspecific cation current and synaptic depression promote network-dependent burst oscillations, *PNAS*, **106** (2009), 2939–2944. https://doi.org/10.1073/pnas.0808776106
10. X. Ding, C. Feng, N. Wang, A. Liu, Q. Xu, Fast-slow dynamics in a memristive ion channel-based bionic circuit, *Cognit. Neurodyn.*, **18** (2024), 3901–3913. https://doi.org/10.1007/s11571-024-10168-z
11. D. Feng, Y. Chen, Q. Ji, Contribution of a Ca^{2+}-activated K^{+} channel to neuronal bursting activities in the Chay model, *Electron. Res. Arch.*, **31** (2023), 7544–7555. https://doi.org/10.3934/era.2023380
12. K. Ma, H. Gu, Z. Zhao, Fast–slow variable dissection with two slow variables: a case study on bifurcations underlying bursting for seizure and spreading depression, *Int. J. Bifurcation Chaos*, **31** (2021), 2150096. https://doi.org/10.1142/s0218127421500966
13. Q. Zhu, M. Li, F. Han, Hopf bifurcation control of the ML neuron model with Hc bifurcation type, *Electron. Res. Arch.*, **30** (2022), 615–632. https://doi.org/10.3934/era.2022032
14. Q. Xu, X. Tan, D. Zhu, H. Bao, Y. Hu, B. Bao, Bifurcations to bursting and spiking in the Chay neuron and their validation in a digital circuit, *Chaos, Solitons Fractals*, **141** (2020), 110353. https://doi.org/10.1016/j.chaos.2020.110353

15. Y. Liu, S. Liu, Canard-induced mixed-mode oscillations and bifurcation analysis in a reduced 3D pyramidal cell model, *Nonlinear Dyn.*, **101** (2020), 531–567. https://doi.org/10.1007/s11071-020-05801-5
16. Y. Xie, Y. Kang, Y. Liu, Y. Wu, Firing properties and synchronization rate in fractional-order Hindmarsh-Rose model neurons, *Sci. China Technol. Sci.*, **57** (2014), 914–922. https://doi.org/10.1007/s11431-014-5531-3
17. L. Guan, H. Gu, X. Zhang, Dynamics of antiphase bursting modulated by the inhibitory synaptic and hyperpolarization-activated cation currents, *Front. Comput. Neurosci.*, **18** (2024), 1303925. https://doi.org/10.3389/fncom.2024.1303925
18. M. Xing, Z. Yang, Y. Chen, Bursting types and bifurcation analysis of the temperature-sensitive Purkinje neuron, *Nonlinear Dyn.*, **111** (2022), 1819–1834. https://doi.org/10.1007/s11071-022-07917-2
19. Q. Wen, S. Liu, B. Lu, Firing patterns and bifurcation analysis of neurons under electromagnetic induction, *Electron. Res. Arch.*, **29** (2021), 3205–3226. https://doi.org/10.3934/era.2021034
20. H. Wang, Q. Wang, Q. Lu, Bursting oscillations, bifurcation and synchronization in neuronal systems, *Chaos, Solitons Fractals*, **44** (2011), 667–675. https://doi.org/10.1016/j.chaos.2011.06.003
21. S. Venugopal, S. Seki, D. H. Terman, A. Pantazis, R. Olcese, M. Wiedau-Pazos, et al., Resurgent Na^+ current offers noise modulation in bursting neurons, *PLoS Comput. Biol.*, **15** (2019), e1007154. https://doi.org/10.1371/journal.pcbi.1007154
22. L. Guan, H. Gu, Y. Jia, Multiple coherence resonances evoked from bursting and the underlying bifurcation mechanism, *Nonlinear Dyn.*, **100** (2020), 3645–3666. https://doi.org/10.1007/s11071-020-05717-0
23. H. Hua, H. Gu, Y. Jia, B. Lu, The nonlinear mechanisms underlying the various stochastic dynamics evoked from different bursting patterns in a neuronal model, *Commun. Nonlinear Sci. Numer. Simul.*, **110** (2022), 106370. https://doi.org/10.1016/j.cnsns.2022.106370
24. B. Hutcheon, Y. Yarom, Resonance, oscillation and the intrinsic frequency preferences of neurons, *Trends Neurosci.*, **23** (2000), 216–222. https://doi.org/10.1016/S0166-2236(00)01547-2
25. R. Wang, H. Gu, X. Zhang, Dynamics of interaction between IH and IKLT currents to mediate double resonances of medial superior olive neurons related to sound localization, *Cognit. Neurodyn.*, **18** (2023), 715–740. https://doi.org/10.1007/s11571-023-10024-6
26. A. I. Tissone, V. B. Vidal, M. S. Nadal, G. Mato, Y. Amarillo, Differential contribution of the subthreshold operating currents I_T, I_h, and I_{Kir} to the resonance of thalamocortical neurons, *J. Neurophysiol.*, **126** (2021), 561–574. https://doi.org/10.1152/jn.00147.2021
27. D. Ulrich, Subthreshold delta ‐ frequency resonance in thalamic reticular neurons, *Eur. J. Neurosci.*, **40** (2014), 2600–2607. https://doi.org/10.1111/ejn.12630
28. R. Narayanan, D. Johnston, Long-term potentiation in rat hippocampal neurons is accompanied by spatially widespread changes in intrinsic oscillatory dynamics and excitability, *Neuron*, **56** (2007), 1061–1075. https://doi.org/10.1016/j.neuron.2007.10.033
29. B. Hutcheon, R. M. Miura, E. Puil, Subthreshold membrane resonance in neocortical neurons, *J. Neurophysiol.*, **76** (1996), 683–697. https://doi.org/10.1152/jn.1996.76.2.683
30. M. W. H. Remme, R. Donato, J. Mikiel-Hunter, J. A. Ballestero, S. Foster, J. Rinzel, et al., Subthreshold resonance properties contribute to the efficient coding of auditory spatial cues, *PNAS*, **111** (2014), E2339–E2348. https://doi.org/10.1073/pnas.1316216111

31. J. Vera, K. Lippmann, Post-stroke epileptogenesis is associated with altered intrinsic properties of hippocampal pyramidal neurons leading to increased theta resonance, *Neurobiol. Dis.*, **156** (2021), 105425. https://doi.org/10.1016/j.nbd.2021.105425
32. B. E. Kalmbach, A. Buchin, B. Long, J. Close, A. Nandi, J. A. Miller, et al., h-channels contribute to divergent intrinsic membrane properties of supragranular pyramidal neurons in human versus mouse cerebral cortex, *Neuron*, 100 (2018), 1194–1208. https://doi.org/10.1016/j.neuron.2018.10.012
33. D. M. Fox, H. A. Tseng, T. G. Smolinski, H. G. Rotstein, F. Nadim, Mechanisms of generation of membrane potential resonance in a neuron with multiple resonant ionic currents, *PLoS Comput. Biol.*, **13** (2017), e1005565. https://doi.org/10.1371/journal.pcbi.1005565
34. J. Mikiel-Hunte, V. Kotak, J. Rinzel, High-frequency resonance in the gerbil medial superior olive, *PLoS Comput. Biol.*, **12** (2016), e1005166. https://doi.org/10.1371/journal.pcbi.1005166
35. H. Hu, K. Vervaeke, J. F. Storm, Two forms of electrical resonance at theta frequencies, generated by M-current, h-current and persistent Na^+ current in rat hippocampal pyramidal cells, *J. Physiol.*, **545** (2002), 783–805. https://doi.org/10.1113/jphysiol.2002.029249
36. N. Binini, F. Talpo, P. Spaiardi, C. Maniezzi, M. Pedrazzoli, F. Raffin, et al., Membrane resonance in pyramidal and GABAergic neurons of the mouse perirhinal cortex, *Front. Cell. Neurosci.*, **15** (2021), 703407. https://doi.org/10.3389/fncel.2021.703407
37. H. G. Rotstein, F. Nadim, Frequency preference in two-dimensional neural models: a linear analysis of the interaction between resonant and amplifying currents, *J. Comput. Neurosci.*, **37** (2013), 9–28. https://doi.org/10.1007/s10827-013-0483-3
38. Z. Zhao, L. Li, H. Gu, Dynamical mechanism of hyperpolarization-activated non-specific cation current induced resonance and spike-timing precision in a neuronal model, *Front. Cell. Neurosci.*, **12** (2018), 62. https://doi.org/10.3389/fncel.2018.00062
39. L. Guan, H. Gu, Z. Zhao, Dynamics of subthreshold and suprathreshold resonance modulated by hyperpolarization-activated cation current in a bursting neuron, *Nonlinear Dyn.*, **104** (2021), 577–601. https://doi.org/10.1007/s11071-021-06230-8
40. K. B. Corbin, F. Harrison, Function of mesencephalic root of fifth cranial nerve, *J. Neurophysiol.*, **3** (1940), 423–435. https://doi.org/10.1152/jn.1940.3.5.423
41. W. Zhang, M. Kobayashi, M. Moritani, Y. Masuda, J. Dong, T. Yagi, et al., An involvement of trigeminal mesencephalic neurons in regulation of occlusal vertical dimension in the guinea pig, *J. Dent. Res.*, **82** (2003), 565–569. https://doi.org/10.1177/154405910308200715
42. Y. Zhao, Y. Liu, J. Wang, Q. Li, Z. Zhang, T. Tu, et al., Activation of the mesencephalic trigeminal nucleus contributes to masseter hyperactivity induced by chronic restraint stress, *Front. Cell. Neurosci.*, **16** (2022), 841133. https://doi.org/10.3389/fncel.2022.841133
43. G. J. Lavigne, S. Khoury, S. Abe, T. Yamaguchi, K. Raphael, Bruxism physiology and pathology: an overview for clinicians, *J. Oral Rehabil.*, **35** (2008), 476–494. https://doi.org/10.1111/j.1365-2842.2008.01881.x
44. N. Wu, A. Enomoto, S. Tanaka, C. F. Hsiao, D. Q. Nykamp, E. Izhikevich, et al., Persistent sodium currents in mesencephalic V neurons participate in burst generation and control of membrane excitability, *J. Neurophysiol.*, **93** (2005), 2710–2722. https://doi.org/10.1152/jn.00636.2004

45. A. Bergmann, D. Edelhoff, O. Schubert, K. J. Erdelt, J. M. P. Duc, Effect of treatment with a full-occlusion biofeedback splint on sleep bruxism and TMD pain: a randomized controlled clinical trial, *Clin. Oral Invest.*, **24** (2020), 4005–4018. https://doi.org/10.1007/s00784-020-03270-z
46. J. Xing, S. Hu, J. Yang, Electrophysiological features of neurons in the mesencephalic trigeminal nuclei, *Neurosignals*, **22** (2015), 79–91. https://doi.org/10.1159/000369822
47. N. Wu, C. F. Hsiao, S. H. Chandler, Membrane resonance and subthreshold membrane oscillations in mesencephalic V neurons: participants in burst generation, *J. Neurosci.*, **21** (2001), 3729–3739. https://doi.org/10.1523/JNEUROSCI.21-11-03729.2001
48. S. Seki, T. Yamamoto, K. Quinn, I. Spigelman, A. Pantazis, R. Olcese, et al., Circuit-specific early impairment of proprioceptive sensory neurons in the SOD1G93A mouse model for ALS, *J. Neurosci.*, **39** (2019), 8798–8815. https://doi.org/10.1523/jneurosci.1214-19.2019
49. M. La Rosa, M. I. Rabinovich, R. Huerta, H. D. I. Abarbanel, L. Fortuna, Slow regularization through chaotic oscillation transfer in an unidirectional chain of Hindmarsh-Rose models, *Phys. Lett. A*, **266** (2000), 88–93. https://doi.org/10.1016/S0375-9601(00)00015-3

Appendix

For $I_{\text{app}} = -7$ pA, the subthreshold oscillations with an amplitude of approximately 13 mV appear, as illustrated in Figure A1(a). The oscillation frequency is about 90.9 Hz. For the fast subsystem, the bifurcations with respect to h_{p} are illustrated in Figure A1(b), similar to those of $I_{\text{app}} = -5$ pA [Figure 5(a)]. So we omit the detailed descriptions here. The three key bifurcation points, Hopf, LPC1, and LPC2, occur at $h_{\text{p}} \approx 0.567897$, 0.581541, and 0.583842, respectively. Then, the trajectory of the subthreshold oscillation (solid black curve) is added to the bifurcations in the (h_{p}, V) plane. Obviously, the trajectory operates on a stable limit cycle with a lower amplitude, as shown by the enlarged view in Figure A1(b).

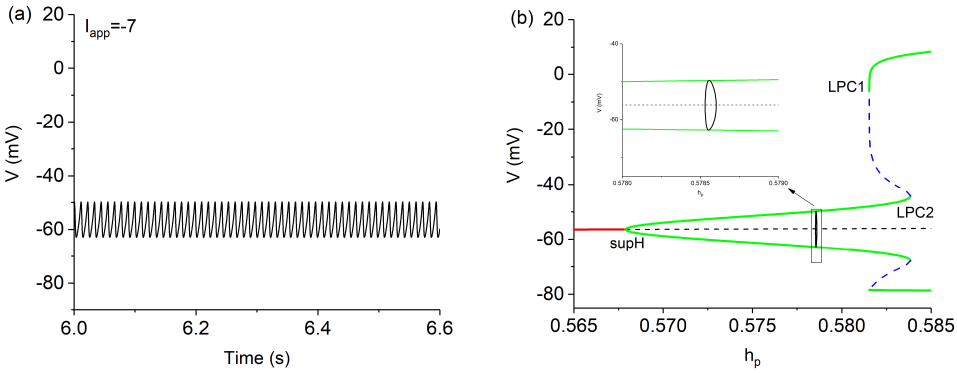

Figure A1. Fast-slow variable analysis of subthreshold oscillation for $g_{\text{NaP}} = 1.1$ nS, $I_{\text{app}} = -7$ pA, and $g_{\text{K}} = 6$ nS. (a) Membrane voltage. (b) The phase trajectory (black curve and the insert) is plotted with bifurcations of the fast subsystem. Symbols are the same as in Figure 5(a).